Wind-induced chaotic mixing in a two-layer density stratified shallow flow

Wind-induced Chaotic Mixing in A Two-layer Density-stratified Shallow Flow

ABSTRACT

Tracer dynamics are computed for a shallow two-layer flow in a circular basin subjected to alternating wind-induced circulation. Lagrangian particle tracking is used to model the dynamics of passive tracers in both the upper and lower layers of a flow with distinct two-layer structure. Results show that particle advection becomes chaotic in parts of the flow in both layers where the effect of external forcing is concentrated primarily in the upper layer, with particles in the lower layer less mixed.

Keywords: chaotic mixing, density-stratification, Kranenburg's basin, Lagrangian tracking, two-layer lakes & reservoirs, shallow flows.

1 Introduction

The phenomenon of Lagrangian chaos has been a subject of great interest following the landmark demonstration by Aref (1984) that extremely complicated particle motions can occur in relatively simple unsteady flow fields. Its relevance to environmental flow in the shallow water regime, such as can occur in wide rivers, lakes, coastal lagoons and estuaries, is of crucial importance to the overall water quality and the well-being of aquatic eco-systems. At the time of writing, the dynamical system approach is widely used in the study of mixing and transport in environmental fluid flows, and comprehensive reviews have been reported by, amongst others, Wiggins (2005), Koshel & Prants (2006), Károlyi *et al.* (2010), and more recently by Prants (2013).

For bounded flows such as occur in lakes and basins, internal circulation is typically driven by wind shear. Temperature-driven stratified structures are also commonly found. Such stratification is typically characterised by a layered structure with each layer having a distinct density. Due to the cyclic rise and fall of the layer interface, tracers released from a fixed location may be entrained into either the upper or lower layer. In the absence of vigorous vertical stirring, and noting that the flow dynamics of the two layers (arising from geographical and bathymetric features) may be very different, the tracers may thus be confined to horizontal mixing in either layer and so are subjected to dissimilar fates.

Following the extensive study on chaotic analysis of surface pollutants in environmental fluids (Zimmerman 1986, Budyansky *et al.* 2007, Liang *et al.* 2006a,b, Pattantyús-Ábrahám *et al*. 2008), pioneering work on chaotic mixing in layered liquid has also been reported,

though restricted to idealised point vortex flow (Ryzhov & Koshel 2012, Sokolovskiy *et al.* 2013, Koshel *et al.* 2013). In this paper, we consider the phenomenon of wind-induced chaotic advection in a two-layer density-stratified shallow water regime, where the flow field is derived from a two-layer shallow flow model using a second-order Roe-type finite volume scheme (Lee *et al.* 2011). Lagrangian particle tracking is then performed at both the surface and lower layers to contrast the dynamics and eventual fate of tracers in either layer. The results are presented in the form of Poincaré sections, and advection tracks of a numerical tracer line.

2 Two-layer Kranenburg's basin

Shallow water flows often involve horizontal circulation zones confined within the surface layer. Such gyres are typically driven by wind stress acting on the surface of the water bodies. The resulting flow is largely dependent on the bathymetry, hence the term topographic gyres. Chaotic particle motions in a shallow water lake model subjected to time varying wind action were first considered by (Kranenburg 1990), and then extended to different bed configurations (Liang *et al.* 2006a), and basin geometries (Liang *et al.* 2006b, Pattantyús-Ábrahám *et al.* 2008). In general, the results confirm that the particle motions change from regular to chaotic as the dimensionless storm duration increases. The presence of internal hyperbolic point(s) and coherent structures such as manifolds is reported to act as Lagrangian barriers that hinder local material transfer in the transverse direction, while providing avenues of streamwise transport (Pattantyús-Ábrahám *et al.* 2008).

For lakes with a layered structure, such as a cold layer beneath a warm layer, or salt water beneath fresh water, an internal seiche may take over the role of the free surface, though with relatively larger motion compared to an ordinary surface seiche. There are two primary modes of motion: the barotropic mode which is essentially identical to the motion of a homogeneous fluid, and the baroclinic mode arising from the density difference in the vertical water column. A two-layer model is sufficient to capture the dynamics of the motion since the contributions of the higher baroclinic modes are typically negligible (Csanady 1975). Since the barotropic motion is more directly affected by the depth variations (i.e. feel the bottom more, leading to the development of so-called topographic gyres), particles in the upper and lower layers are likely to experience different fates under wind-dominant lake circulation.

Consider Kranenburg's circular shallow basin (Kranenburg 1990) for which the still water depth h_s, as a function of the radial distance R from the basin's centre, is given by:

$$h_s = H\left(\frac{1}{2} + \sqrt{\frac{1}{2}(1 - \frac{R}{R_0})}\right) \tag{1}$$

where the basin characteristic length R_0 is 120 m and weighted mean water depth H is 0.5 m (Fig. 1), and the upper layer has a uniform thickness equivalent to one-fifth the maximum depth at the centre of the basin.

Here, the flow field is a weak system governed by a single parameter related to the storm duration t_s. The dimensionless storm duration parameter Γ (Kranenburg 1990) is defined as

$$\frac{\ln Z}{8\kappa}\frac{u_* t_s}{R_0} \tag{2}$$

where $Z = H/z_0$, $z_0 = 2.8$ mm is the roughness height of the bed, u_* is the friction velocity at the free surface, and $\kappa = 0.4$ is the von Kármán constant.

3 Two-layer shallow water model

The hydrodynamics of the two-layer Kranenburg's basin is described using a two superposed immiscible layers of shallow water fluids described by the two-layer shallow water equations in the form of a hyperbolic system with non-conservative products and source terms (Lee *et al.* 2011):

$$\mathbf{W}_t + \mathbf{F}_1(\mathbf{W})_x + \mathbf{F}_2(\mathbf{W})_y = \mathbf{B}_1(\mathbf{W})\mathbf{W}_x + \mathbf{B}_2(\mathbf{W})\mathbf{W}_y + \mathbf{S}_1(x,\mathbf{W}) + \mathbf{S}_2(y,\mathbf{W}),$$

where the subscripts x, y and t denote partial derivatives with respect to the x-direction, y-direction, and time. The vector of unknowns, $\mathbf{W}$, the flux function vectors, $\mathbf{F}_1$ and $\mathbf{F}_2$, the source term vectors which describe the variable bed topography, $\mathbf{S}_1$ and $\mathbf{S}_2$, and the coupling matrices $\mathbf{B}_1$ and $\mathbf{B}_2$ are defined as:

$$\mathbf{W} = \mathbf{W}(x,y,t) = \begin{bmatrix} W_1(x,y,t) \\ W_2(x,y,t) \end{bmatrix}, W_j = \left[h_j, q_{x,j}, q_{y,j}\right]^T,$$

$$\mathbf{F}_1 = \mathbf{F}_1(x,y,t) = \begin{bmatrix} F_{1,1}(W_1) \\ F_{1,2}(W_2) \end{bmatrix}, \quad F_{1,j} = \begin{bmatrix} q_{x,j} \\ q_{x,j}^2/h_j + gh_j^2/2 \\ q_{x,j}q_{y,j}/h_j \end{bmatrix},$$

$$\mathbf{F}_2 = \mathbf{F}_2(x,y,t) = \begin{bmatrix} F_{2,1}(W_1) \\ F_{2,2}(W_2) \end{bmatrix}, \quad F_{2,j} = \begin{bmatrix} q_{y,j} \\ q_{x,j}q_{y,j}/h_j \\ q_{y,j}^2/h_j + gh_j^2/2 \end{bmatrix},$$

$$\mathbf{S}_1 = \mathbf{S}(x,\mathbf{W}) = \begin{bmatrix} S_{1,1}(x,W_1) \\ S_{1,2}(x,W_2) \end{bmatrix}, \quad S_{1,j} = \left[0, -gh_j b(x,y)_x, 0\right]^T,$$

$$\mathbf{S}_2 = \mathbf{S}(y,\mathbf{W}) = \begin{bmatrix} S_{2,1}(y,W_1) \\ S_{2,2}(y,W_2) \end{bmatrix}, \quad S_{2,j} = \left[0, 0, -gh_j b(x,y)_y\right]^T,$$

$$\mathbf{B}_1(\mathbf{W}) = \begin{bmatrix} 0 & B_{1,1}(W_1) \\ B_{1,2}(W_2) & 0 \end{bmatrix},$$

$$\mathbf{B}_2(\mathbf{W}) = \begin{bmatrix} 0 & B_{2,1}(W_1) \\ B_{2,2}(W_2) & 0 \end{bmatrix},$$

where

$$B_{1,1}(W_1) = \begin{bmatrix} 0 & 0 & 0 \\ -gh_1 & 0 & 0 \\ 0 & 0 & 0 \end{bmatrix}, \qquad B_{1,2}(W_2) = \begin{bmatrix} 0 & 0 & 0 \\ -rgh_2 & 0 & 0 \\ 0 & 0 & 0 \end{bmatrix},$$

$$B_{2,1}(W_2) = \begin{bmatrix} 0 & 0 & 0 \\ 0 & 0 & 0 \\ -gh_1 & 0 & 0 \end{bmatrix}, \qquad B_{2,2}(W_2) = \begin{bmatrix} 0 & 0 & 0 \\ 0 & 0 & 0 \\ -rgh_2 & 0 & 0 \end{bmatrix}.$$

The flow rate components $q_{x,j}(x,y,t)$ and $q_{y,j}(x,y,t)$ and the layer thickness $h_j(x,y,t)$ are the dependent variables, $b(x,y)$ is the bed elevation measured from a reference horizontal datum. The subscript j denotes the layers, where index 1 and 2 refers to the upper layer and the lower layer respectively, such that the densities of each layer are given by $(\rho_1,\rho_2) = (1000,1020)$ (i.e. density ratio $r = 0.98$, and $g = 9.81\text{m/s}^2$).

The numerical scheme is a second-order Roe-type finite volume scheme. We assume that the system is strictly hyperbolic, i.e. there are 6 distinct eigenvalues λ_i, $i = 1, 2 \ldots 6$ in each of the x- and y-directions respectively such that the corresponding eigenvectors are linearly independent. Two of the eivenvalues are given by the velocities in the respective layers $U_j, j = 1,2$. The remaining four eigenvalues are determined using the characteristic equation derived from the system matrix:

$$(\lambda^2 - 2U_1\lambda + U_1^2 - gh_1)(\lambda^2 - 2U_2\lambda + U_2^2 - gh_2) = rg^2h_1h_2.$$

Our interest lies mainly in the case when $r \approx 1$, which is common in stratified water bodies. Hence, the first order approximation of the eigenvalues can be written as (Schijf and Sconfeld 1953):

$$\lambda_{\text{ext}} = \frac{h_1U_1 + h_2U_2}{h_T} \pm \sqrt{gh_T},$$

$$\lambda_{\text{int}} = \frac{h_1U_2 + h_2U_1}{h_T} \pm \sqrt{\frac{g'h_1h_2}{h_T}\left(1 - \frac{(U_2 - U_1)^2}{g'h_T}\right)}$$

where $h_T = h_1 + h_2$ and $g' = g(1-r)$ is the reduced gravity.

The external eigenvalues λ_{ext} and the internal eigenvalues λ_{int} are related respectively to barotropic and baroclinic components of the flow, noting that the values of the internal eigenvalues are much lower in comparison. If the solution yields four different real eigenvalues, the flow is stable and the system is hyperbolic. This requires the approximated condition

$$(U_2 - U_1)^2 / g' h_T < 1$$

to be satisfied, i.e. the velocity difference between the layers must be small. Violation of the hyperbolic condition produces numerical disturbance which tends to grow and eventually to overwhelm the solution unless the viscous effect is added.

The bed stress is evaluated empirically, with the bed roughness coefficient C_b estimated from $C_b = [\kappa/(1+\ln(z_0/h_j))]^2$ in which h_j is the instantaneous depth of the layer in contact with the bed, and the layer-averaged eddy viscosity is given by $\varepsilon = \kappa u_* h_j / 6$. The interfacial stress is evaluated using an interface friction coefficient $C_f = 0.03$ whose value was set arbitrarily. Equivalent wind stress on the lower layer is given by $-\tau_w h_2/(h_1+h_2)$, and the effect of the Earth's rotation is ignored.

4 Wind-induced circulation

In order to resolve the velocity field near the domain boundary more accurately, we apply a quadtree grid system (see e.g. Liang *et al.* 2006a, Lee *et al.* 2011) where grid sizes are refined systematically to fit better to the circular domain boundary. Considering a constant wind shear stress $\tau_w = 2.0\times10^{-3}$ Nm^{-2} in the north-west direction, applied uniformly throughout the entire domain, the simulations are run until steady state condition is reached using a no-slip boundary condition. The time step $\Delta t = 0.1$ s.

The resulting steady-state streamline contours are as shown in Fig. 2. Both the upper and lower layers span across the entire domain and share the same boundary which is essentially vertical at the basin perimeter. The streamlines of both layers are similar, with the pairs of topographic gyres in each layer separated by a dividing streamline located diametrically across the basin and parallel to the wind direction. Along this axis of symmetry, the velocities in the upper layer are directed against the wind, whereas those in the lower layer are in the same direction as the wind. As these upwind and downwind flows of the upper and lower layers, respectively, reach the far end of the basin, they turn around along the shallow area near the basin perimeter, creating a rapid jet of flow along the shore in the opposite direction -- similar to that observed in a single layer model (Liang *et al.* 2006a, Kranenburg 1990), and consistent with (Csanady 1975), who noted that for uniformly distributed wind shear, depth-

averaged velocities are directed with the wind in the shallow region, and against the wind in the deep region.

The overall consequence of these flows is essentially an internal set-up/ set-down, which is common in a stratified lake. The interface separating the layers sinks at the downwind section and rises at the upwind section. The balanced internal forces cause the free surface to remain near horizontal with negligible surface gradient. At a density ratio closer to unity, e.g. r = 0.99, the lower layer is observed to outcrop the surface of the upper layer. This is however not considered in the present study.

We note that the applied wind shear stress is relatively small, thus circumventing the perturbation arising from surface wave action and internal shear at the interface. As a result, the steady state condition is only reached after an extended time period. Furthermore, wind shear is assumed to be uniform over the entire basin. From the meteorological point of view, this is likely for coastal lagoons or basins which are exposed to long-term periodic wind forcing. In the present context, we further assume uniform wind magnitude which alternates from two dominant directions. Essentially, we illustrate a highly idealized case of possible chaotic mixing in a basin subjected to low perturbation of high regularity.

5 Lagrangian particle tracking

In order to obtain the Lagrangian particle paths, time-integration of the advection equations is performed using a Runge-Kutta Cash-Karp algorithm with the Eulerian velocity field provided by the two-layer shallow water solver described in the preceding section. The steady state flow field as shown in Fig.2 is applied from the beginning of the simulation. The wind periodicity T varies according to t_s, where three different storm durations t_s are considered, corresponding to dimensionless storm duration parameters Γ = 0.14, 0.28 and 0.84. In each case, at half-period intervals $T/2$, the wind direction is abruptly switched between the north-east and north-west directions alternately. Here, the Eulerian velocity field is assumed to adapt instantaneously to the wind conditions. Hence, the orientation of the flow field in Fig.2 is rotated and applied according to the wind direction. Essentially, we now have a simple time-periodic flow which is responsible for the advection of the passive particles in both layers.

The advection equation in a two-dimensional Cartesian coordinate system is expressed as

$$\frac{\mathrm{d}x}{\mathrm{d}t} = u(x, y, t), \quad \frac{\mathrm{d}y}{\mathrm{d}t} = v(x, y, t), \tag{3}$$

where (x,y) is the position of a given particle with respect to an arbitrary origin at time t; and u and v denote the Eulerian velocity components in the x- and y-directions of the flow at the

same spatial and temporal point as the particle. The required continuous velocity field is interpolated linearly across the discretized representation available from adjacent cells of the computational grid. Formally, the equations are integrable for steady and incompressible flow, which is associated with regular advection. On the other hand, for unsteady flow associated with chaotic advection, the equations may be non-integrable.

Despite the use of quadtree grid and no-slip boundary condition to resolve accurately the velocity field near the circular boundary, accurate tracking of particle trajectories in this region remains an inherent numerical challenge due to the rectangular grid system. Hence, we further assume that a particle which tends to cross the domain boundary will be reflected at the normal to the boundary and thus returned to the computational domain. In particular, we have also avoided the zone within 5% of the radius distance from the basin boundary when seeding particle for simulation. We show in Section 6 that particles in the topographic gyres do not traverse the basin shoreline.

Fig. 3 shows the Poincaré sections for tracer particles released along the x-axis in both layers. These plots are generated by plotting the intersections of particle trajectories with the time plane at the end of each period for different dimensionless storm durations $\Gamma = 0.14$, 0.42, 0.70. The particles are tracked for up to 100 cycles. It can be observed that the particle distributions show near-symmetrical symmetry about the vertical axis owing to the alternating wind forcing in the north-westerly and north-easterly directions. However, the symmetry deteriorates at higher dimensionless storm duration which corresponds to more severe weather condition. It should be noted that the phase portrait changes according to when in each period the particle positions are sampled; here, we choose the end of each period.

For $\Gamma = 0.14$, the basin is exactly divided into two regions along the north-south axis. Large islands of regular particle motions can be observed either side of the main axis. Further away from the centres of these islands, the regularity of particle motions degenerates near the main axis and the basin boundary. As Γ increases, the period-one islands diminish in size but remain. The regions away from the islands become increasing chaotic and generally lose their distinctive features. The observations hold for both layers, though regularity in the lower layer persists better, due to the fact that the layer is shielded and is subjected indirectly to reduced shear from the wind forcing. The results are in close agreement with those of single layer models (Kranenburg 1990, Liang *et al.* 2006a).

Chaotic mixing is characterised by stretching and folding, and can be readily visualised by deploying a line of particles in the domain. For this purpose, 10,000 particles are initially uniformly positioned over the interval $[-2R_0/3, 2R_0/3]$ along the x-axis in each layer. For $\Gamma = 0.28$ (Fig. 4), near symmetrical patterns are observed in both layers at times $t = 50T$ and $t =$

100*T*. Particles in the vicinity of the regular islands form two whorl-type structures under the influence of the period-one points. As the line of particles evolves, complicated fractal structures become increasingly visible and the basin is gradually filled with pseudo-stochastic particle tracks. Again, the lower layer lags behind in its time-development due to the reduced effect of the wind forcing compared to the upper layer. At a higher value of $\Gamma = 0.84$ (Fig. 5), particles near the boundary and the main dividing axis are scattered rapidly. The whorl structures in the elliptical zones exhibit much irregular stretching and folding and continue to occupy a significant extent of area in the lower layer even at $t = 100T$, but are heavily encroached by the scattered particles in the upper layer. Hence, good mixing, which is characterised by exponential stretching, is restricted (even at high storm duration) in the lower layer, particularly in the elliptical regions either side of the main axis aligned with the direction of the wind.

We note that although the wind field switches periodically between north-westerly and north-easterly directions, symmetry of the particles' distribution in the basin is lost at the higher storm duration parameter $\Gamma = 0.84$ (Fig. 5) compared to $\Gamma = 0.28$ (Fig. 4). This is because as storm duration increases, particles are advected over longer distances leading to larger spatial divergence, and thus there is an increasing likelihood of being stirred by different gyres at every half-period. Hence, the stirring effect of every first half-cycle becomes increasing difficult to be offset in the second half-cycle, leading to loss of symmetry.

6 Hyperbolic points and invariant manifold

Following the method introduced by Schmelcher and Diakonos (1998), the positions of the hyperbolic points in the domain are found to be identical in both layers, namely H1 and H2, located at (132.6568, 238.3313) and (133.8633, 22.6528) respectively (Fig. 6). The invariant manifolds can be readily observed by performing Lagrangian tracking of particles released at these hyperbolic points. Fig. 7 shows the invariant manifolds in the closed domain. In the upper layer, particles released at the hyperbolic point H1 are observed to escape promptly to the east and west along unstable manifolds parallel to the basin shoreline. These particles travel alongshore towards the hyperbolic point H2 at the south. Nonetheless, they never get close enough to H2 but are deflected towards the stable manifold of H1. This direction of movement is summarised in Fig.6, suggesting that the left and right topographic gyres form independent closed loops. The trend also indicates that particles located between the unstable manifold and the shoreline may be attracted directly to the hyperbolic point H2 and thus possibly are scattered southward.

In the lower layer, particles released at the hyperbolic point H1 are ejected southwards along the unstable manifold which runs through the north-south axis of the basin. As the train of

particles approach hyperbolic point H2, they are stretched and folded, and subsequently escape along the east and west unstable manifolds, moving alongshore and returning to H1. It is interesting to note that as the particles approach H1 again, stretching and folding causes a fraction of them to be ejected from H1 in the northward direction towards the shore, which is not observed in the upper layer.

Since the invariant manifold essentially prohibits material exchange between regions either side of the manifold, it may thus be deduced that there are no interactions between the particles along the annulus of the basin and those in the topographic gyres.

7 Degree of Chaotic mixing

Qualitatively the detailed mixing behaviours in the upper and lower layers are very similar to each other and to that of the one layer model, albeit at lower storm durations for the upper layer and high storm durations for the lower. This simply reflects the rather effective shielding of the lower layer by the upper layer.

In order to quantify particle mixing in the Kranenburg basin, we consider three (3) small particle patches: SQ1 is located at the centre of the basin; SQ2 is located to the southwest; SQ3 is located to the west (see Fig. 6). Each particle patch comprises 4225 particles, arranged in a square shape where the distance between particles is approximately 0.1041. Figs 8 and 9 show the temporal growth of the mean and standard deviation of the particle distances in the upper layer, subjected to storm duration parameter $\Gamma = 0.28$ and 0.84 respectively. In both cases, based on the results for wind forcing up to 75 cycles, particle patch SQ1 is the most mixed, whereas SQ3 is the least mixed, which agrees well with the observations of the preceding Poincaré sections. For SQ1, the mean particle distance after 75 cycles increased from approximately 16 for $\Gamma = 0.28$, to over 100 for $\Gamma = 0.84$. Meanwhile, the standard deviation of the particle distance also more than doubled from about 25 to over 60. It is also observed that the mean and standard deviation of the particle distance approaches steady state after 75 cycles for the case $\Gamma = 0.84$, but is still rising slowly for the case $\Gamma = 0.28$ due to the relatively low perturbation. The fact that the mean particle distance has increased by over 1000 times for the case of $\Gamma = 0.84$ suggests significant divergence of initially nearby particles. However, owing to the relatively long time period, the finite-size Lyapunov exponents (Károlyi *et al.* 2010) in a large fraction of the basin area, though positive, have very small values.

Turning to particles in the lower layer, the mean distances reduce by approximately 50% and 20% for $\Gamma = 0.28$ and $\Gamma = 0.84$ respectively at the end of 75 cycles (figure not shown). Meanwhile, the standard deviation of the particle distances remains identical to that of the upper layer.

8 Conclusions

Chaotic mixing has been investigated in a two-layer density-stratified shallow water flow. The flow field is generated using a second-order Roe-type finite volume scheme, and individual particle fates tracked using a Lagrangian technique. For wind-induced circulation in Kranenburg's basin with a two-layer stratified flow structure, it is found that chaotic mixing of the surface and lower layer follow similar patterns, though the lower layer is less mixed owing to the shielding effect from the external wind shear. In future work, it would be interesting to compute the growth in time of a line of particles and its fractal dimension. Overall, the study reveals interesting mixing features in a density-stratified flow, which would be otherwise obscured in a depth-averaged shallow water model.

Acknowledgements

The research is partly funded by Malaysian Ministry of Higher Education Fundamental Research Grant Scheme (FRGS) and Research Management Institute (RMI), Universiti Teknologi MARA, Malaysia (Ref: FRGS /1/2012/TK03/UiTM/03/6).

Notation

$(\mathbf{B}_1, \mathbf{B}_2)$ = coupling matrices
b = bed elevation [m]
C_b = bed roughness coefficient [-]
C_f = interface friction coefficient [-]
$(\mathbf{F}_1, \mathbf{F}_2)$ = flux function vectors
g = acceleration due to gravity [m/s^2]
g' = reduced gravity [m/s^2]
H = weighted mean water depth [m]
h_j = instantaneous water depth of layer j [m]
h_s = still water depth [m]
h_T = total water depth (= $h_1 + h_2$) [m]
q = flow rate [m^3/s]
R = radial distance (from centre of the circular basin) [m]
R_0 = basin characteristic length [m]
$(\mathbf{S}_1, \mathbf{S}_2)$ = vectors of source terms
r = density ratio [-]
T = storm period [s]
t_s = storm duration [s]
U = layer velocity [m/s]

(u,v) = velocity components in the x- and y-directions respectively [m/s]

u_* = friction velocity [m/s]

$\mathbf{W}$ = vector of dependent variables

(x,y) = Cartesian coordinate [m]

Z = ratio of weighted mean water depth to roughness height [-]

z_0 = roughness height

ε = depth-averaged eddy viscosity [m^2/s]

Δt = time step [s]

Γ = dimensionless storm duration parameter [-]

κ = von Kármán constant [-]

λ = eigenvalue

(ρ_1,ρ_2) = densities of the upper and lower layers [kg/m^3]

τ_w = wind shear stress [N/m^2]

References

Aref, H. (1984). Stirring by chaotic advection. *J. Fluid Mech.*, 143, 1–21.

Budyansky, M. V., Uleysky, M. Y., Prants, S. V. (2007). Lagrangian coherent structures, transport and chaotic mixing in simple kinematic ocean models. *Commun. Nonlinear Sci. Numer. Simul.*, 12 (1), 31-44.

Csanady, G. T. (1975). Hydrodynamics of large lakes. *Ann. Rev. Fluid Mech.*, 7, 357–386.

Károlyi, G., Pattantyús-Ábrahám, M., Krámer, T., Józsa, J., Tél, T. (2010). Finite-size Lyapunov exponents: a new tool for lake dynamics. *Proc. Inst. Civil Eng., Eng. Comp. Mech.,* 63(EM4), 251-259.

Kranenburg, C. (1990). Wind-driven chaotic advection in a shallow model lake. *J. Hydraul. Res.*, 30 (1), 29–46.

Koshel, K.V., Prants, S.V. (2006). Chaotic advection in the ocean. *Physics-Uspekhi*, 49(11), 1151-1178.

Koshel, K.V., Sokolovskiy, M. A., Verron, J. (2013). Three-vortex quasi-geostrophic dynamics in a two-layer fluid. Part 2. Regular and chaotic advection around the perturbed steady states. *J. Fluid Mech.*, 717, 255-280.

Lee, W.K., Taylor, P.H., Borthwick, A.G.L. & Chuenkhum, S. (2010). Vortex-induced chaotic mixing in wavy channels. *J. Fluid Mech.*, 654, 501-538.

Lee, W. K., Borthwick, A. G. L., Taylor, P. H. (2011). A fast adaptive quadtree scheme for a two-layer shallow water model. *J. Comput. Phys.*, 230, 4848-4870.

Liang, Q., Borthwick, A. G. L., Taylor, P. H. (2006a). Wind-induced chaotic advection in shallow flow geometries. Part I: Circular basins. *J. Hydraul. Res.*, 44 (2), 170-179.

Liang, Q., Borthwick, A. G. L., Taylor, P. H. (2006b). Wind-induced chaotic advection in shallow flow geometries. Part I: Non-circular basins. *J. Hydraul. Res.*, 44 (2), 180-188.

Pattantyús-Ábrahám, M., Tél, T., Krámer, T., Józsa, J. (2008). Mixing properties of a shallow basin due to wind-induced chaotic flow. *Adv. Water Res.*, 31 (3), 525-534.

Prants, S.V. (2013). Dynamical systems theory methods to study mixing and transport in the ocean. *Physica Scripta*, 87, 038115 (12pp).

Ryzhov, E.A., Koshel, K.V. (2012). Interaction of a monopole vortex with an isolated topographic feature in a three-layer geophysical flow. *Nonlin. Processes Geophys.*, 20(1), 107-119.

Schijf, J.B., Schonfeld, J.C. (1953). Theoretical considerations on the motion of salt and fresh water. In: *Proc. of the Minn. Int. Hydraul. Conv.*, Joint meeting IAHR and Hyd. Div. ASCE., 321-333.

Schmelcher P., Diakonos F.K. (1998). General approach to the localization of unstable periodic orbits in chaotic dynamics systems. *Phys. Rev. E*, 57 (3), 2739-2746.

Sokolovskiy M. A., Koshel K.V., Verron, J. (2013). Three-vortex quasi-geostrophic dynamics in a two-layer fluid. Part 1. Analysis of relative and absolute motions. *J. Fluid Mech.*, 717, 232-254.

Wiggins, S. (2005). The dynamical systems approach to Lagrangian transport in oceanic flows. *An. Rev. Fluid Mech.*, 37, 295-328.

Zimmerman, J. T. F. (1986). The tidal whirlpool: A review of horizontal dispersion by tidal and residual currents. *Neth. J. Sea Res.*, 20 (2-3), 133-154.

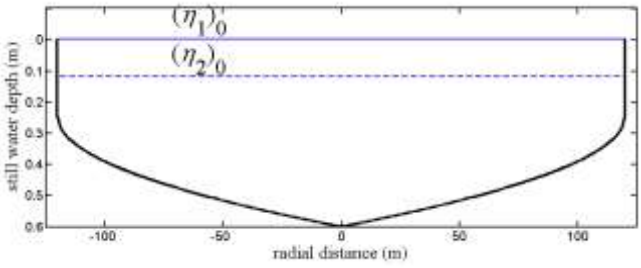

Figure 1: Cross section of Kranenburg's (1990) basin, showing initial profiles of the free surface $(\eta_1)_0$ and the interface $(\eta_2)_0$.

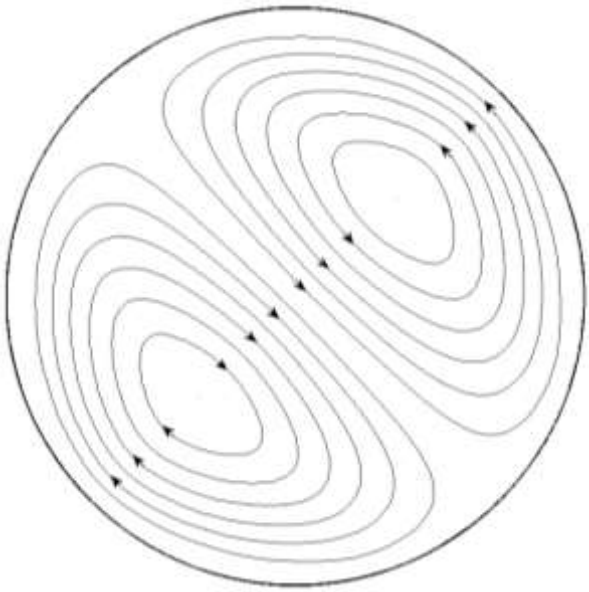

Figure 2: Steady state streamlines due to north-westerly wind.

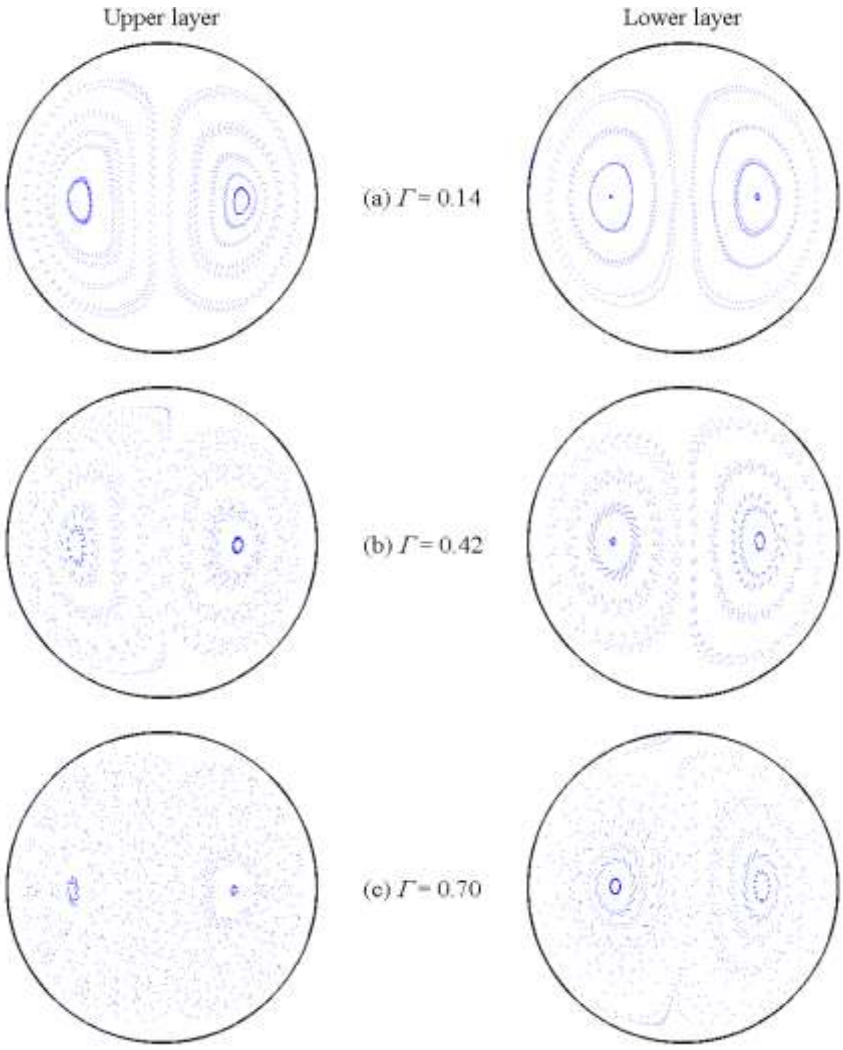

Figure 3: Poincaré sections for different dimensionless storm durations.

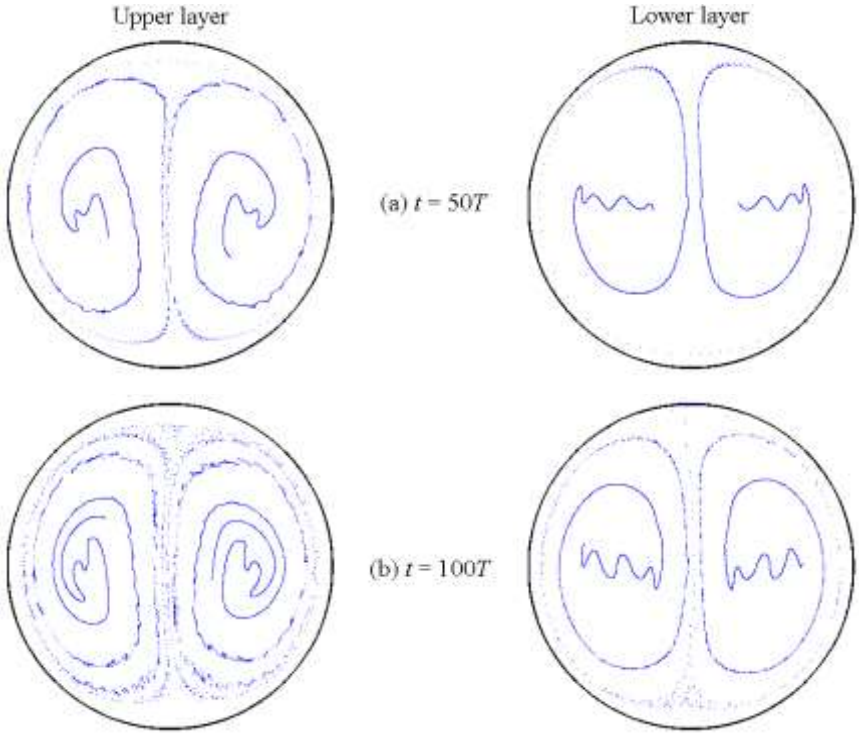

Figure 4: Advection of a line of particles for $\Gamma = 0.28$.

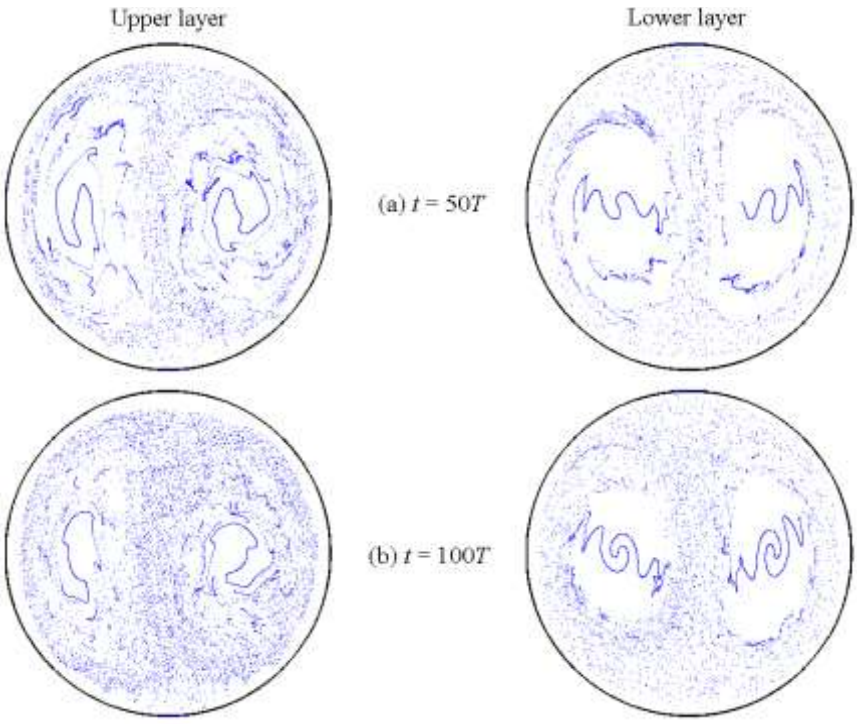

Figure 5: Advection of a line of particles for $\Gamma = 0.84$.

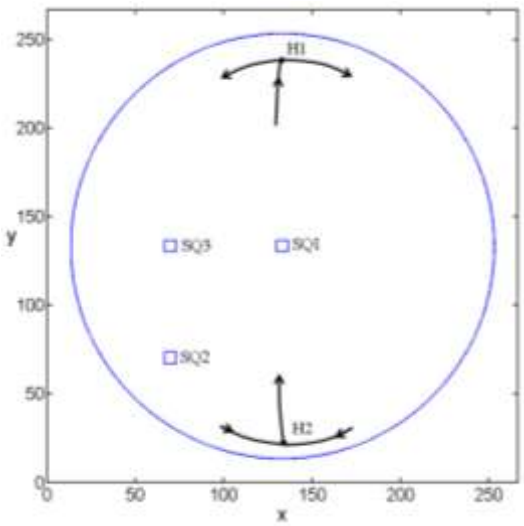

Figure 6: The hyperbolic points H1 and H2 (indicated by •): arrow showing direction of particle movement on the upper layer. Also showing initial positions of small particle patch: SQ1, SQ2 and SQ3

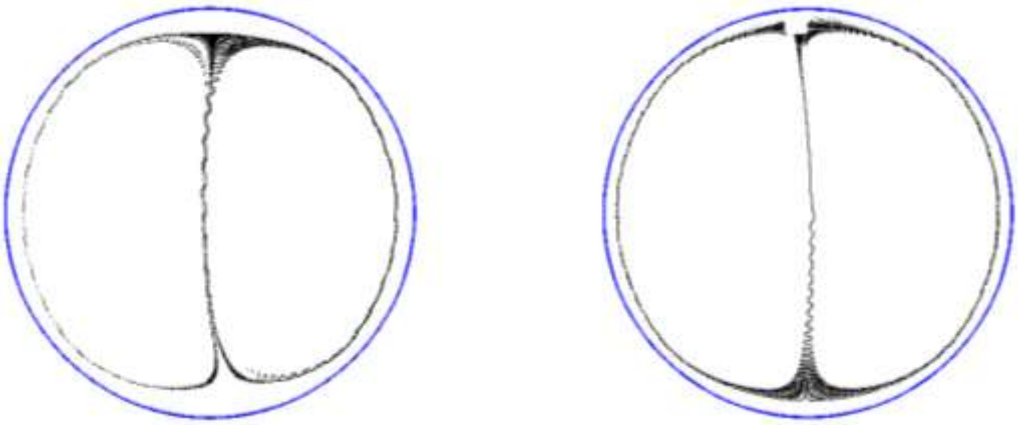

Figure 7: The invariant manifold in the upper (left) and lower (right) layer, traced by particles released at the hyperbolic points H1 and H2 and tracked up to 100 cycles.

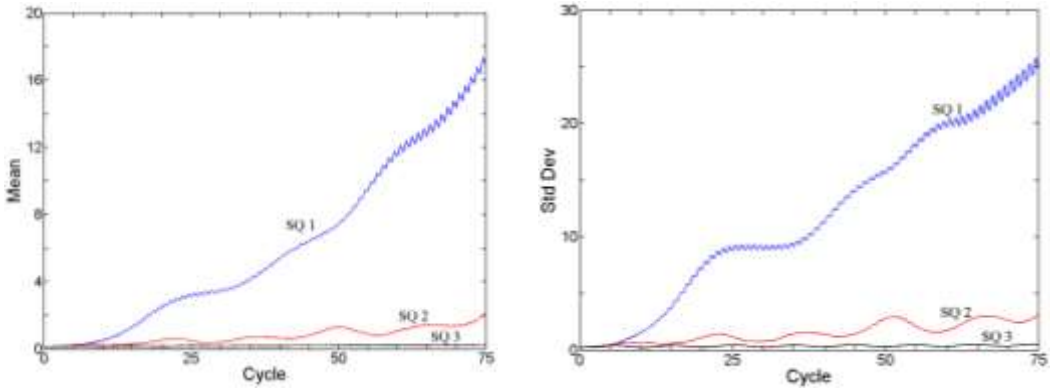

Figure 8: Spreading of small particle patch in the upper layer: Temporal growth of mean (left) and standard deviation (right) of particle distances for the case $\Gamma = 0.28$.

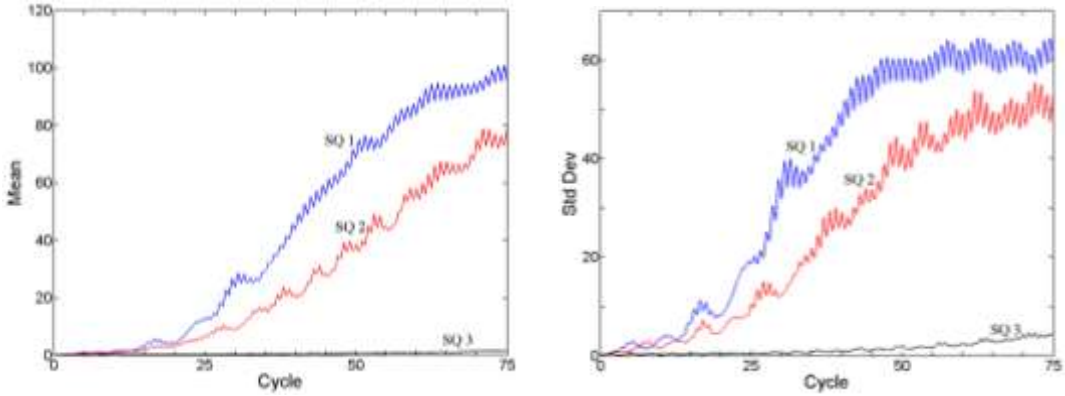

Figure 9: Spreading of small particle patch in the upper layer: Temporal growth of mean (left) and standard deviation (right) of particle distances for the case $\Gamma = 0.84$.